

## Cryogenic merged-ion-beam experiments in DESIREE: Final-state-resolved mutual neutralization of $\text{Li}^+$ and $\text{D}^-$

Gustav Eklund <sup>1,\*</sup>, Jon Grumer <sup>2</sup>, Stefan Rosén,<sup>1</sup> MingChao Ji <sup>1</sup>, Najeeb Punnakayathil <sup>1</sup>, Anders Källberg,<sup>1</sup> Ansgar Simonsson <sup>1</sup>, Richard D. Thomas,<sup>1</sup> Mark H. Stockett,<sup>1</sup> Peter Reinhed,<sup>1</sup> Patrik Löfgren,<sup>1</sup> Mikael Björkhage,<sup>1</sup> Mikael Blom <sup>1</sup>, Paul S. Barklem <sup>2</sup>, Henrik Cederquist <sup>1</sup>, Henning Zettergren,<sup>1</sup> and Henning T. Schmidt <sup>1,†</sup>

<sup>1</sup>Department of Physics, Stockholm University, Stockholm 10691, Sweden

<sup>2</sup>Department of Physics and Astronomy, Uppsala University, Uppsala 75237, Sweden



(Received 24 March 2020; accepted 29 June 2020; published 30 July 2020)

We have developed an experimental technique to study charge- and energy-flow processes in sub-eV collisions between oppositely charged, internally cold, ions of atoms, molecules, and clusters. Two ion beams are stored in separate rings of the cryogenic ion-beam storage facility DESIREE, and merged in a common straight section where a set of biased drift tubes is used to control the center-of-mass collision energy locally in fine steps. Here, we present measurements on mutual neutralization between  $\text{Li}^+$  and  $\text{D}^-$  where a time-sensitive imaging-detector system is used to measure the three-dimensional distance between the neutral Li and D atoms as they reach the detector. This scheme allows for direct measurements of kinetic-energy releases, and here it reveals separate populations of the  $3s$  state and the  $(3p + 3d)$  states in neutral Li while the D atom is left in its ground state  $1s$ . The branching fraction of the  $3s$  final state is measured to be  $57.8 \pm 0.7\%$  at a center-of-mass collision energy of  $78 \pm 13$  meV. The technique paves the way for studies of charge-, energy-, and mass-transfer reactions in single collisions involving molecular and cluster ions in well-defined quantum states.

DOI: [10.1103/PhysRevA.102.012823](https://doi.org/10.1103/PhysRevA.102.012823)

### I. INTRODUCTION

Charge- and energy-transfer processes in collisions between atomic systems have been studied since the early days of quantum mechanics [1,2]. The main motivation has been to understand the reaction mechanisms, and ultimately to determine the corresponding reaction rates. The latter are of large practical interest in a wide range of fields including studies of comets [3,4], planetary [5,6] and stellar atmospheres [7,8], and other astrophysical [9] and fusion [10] plasma. Furthermore, charge- and energy-transfer processes occur in chemical reactions in the gas phase [11] and in solution (see, e.g., Ref. [12]), and they are important to understand for medical radiation therapy and for radiation protection (see, e.g., Ref. [13]). There is an enormous body of data based on fundamental studies of charge- and energy-transfer processes where a single isolated atomic system interacts (collides) once with another such system in vacuum [14]. A large fraction of these studies have been performed with positively charged ions at energies ranging from a few eV and up, while results on collisions with neutrals and anions in the same energy range are somewhat less abundant but

still extensive. At extremely low energies, interactions among ultracold atoms on the nanokelvin scale have been extensively studied since the 1990s [15]. In comparison, data are still very scarce in the intermediate meV collision energy range and for systems where two ionized systems interact. Such studies are important for the modeling of cold interstellar media [16] and of other astrophysical environments [17]. By controlling the internal quantum states, comparisons with theoretical calculations become much more straightforward.

Major steps forward in the understanding of atomic reaction mechanisms have often been taken in connection with the inventions of new experimental, theoretical, and computational techniques. An early breakthrough on the instrumental side involves the ability to investigate the outcome of single individual reactions, which requires a low enough base pressure and the ability to count (and identify) the separate reaction products. Reaction microscopy [18,19] and the possibility to perform kinematically complete experiments where the momentum vectors of all outgoing reaction products can be registered with high resolution revolutionized the field of atomic collision physics in the 1990s. A vast number of studies have since been performed using this technique. One example, which connects back to the very early days of quantum mechanics, concerns the Thomas electron-capture mechanism in fast atomic collisions [1]. This mechanism, in which one electron in the target first scatters on the fast projectile and then scatters on the target nucleus such that it is captured to the projectile, produces a characteristic projectile scattering angle and a characteristic momentum of the recoiling target nucleus. For fast proton-He collisions, an experimental indication of the process was first reported in the 1980s [20], but

\*gustav eklund@fysik.su.se

†henning.schmidt@fysik.su.se

Published by the American Physical Society under the terms of the Creative Commons Attribution 4.0 International license. Further distribution of this work must maintain attribution to the author(s) and the published article's title, journal citation, and DOI. Funded by Bibsam.

it was only through recoil ion momentum spectroscopy that the Thomas mechanism could be fully separated from other electron-transfer mechanisms [21].

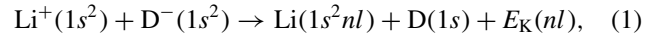
Furthermore, in the 1990s other key instrumental developments made it possible to study atomic collisions with ions stored at high velocities in *magnetic* ion-beam storage rings operating at *room temperature* [22–25]. Using electron-ion merged-beams techniques, this brought new insights into how free electrons interact with atomic and molecular ions at very low collision energies [26]. Ideally, however, studies of atomic collisions should be made with full control of the quantum states of the collision partners before and after the collision. This is in general very difficult or even impossible to achieve in room-temperature devices. Here we focus on ion-ion collisions and for this we have developed the Double Electrostatic Ion Ring Experiment (DESIREE) [27,28] facility for operation at *cryogenic temperatures*. This device is designed to enable the first merged-beams experiments with two stored ion beams. Merged-beams studies provide a level of control over the collision energy which is not possible with other methods [29]. The storage in the cryogenic environment allows for control of the ions' internal excitation prior to their interactions by storing them for up to hours [30] and waiting for spontaneous relaxation or actively manipulating the distribution on quantum levels [31].

In this paper we report the results of a merged-beams experiment with two stored ion beams. This pilot experiment is performed with  $\text{Li}^+$  and  $\text{D}^-$  in their lowest quantum states. We measure the kinetic-energy-release distribution for the mutual neutralization (MN) reactions, which reveals the final quantum-state distributions of the Li and D neutral products. Depending on the internal quantum level schemes, charge-exchange experiments may sometimes be performed with pure ground-state ion beams for atomic ions even at room temperature [32]. This is virtually impossible for studies of collisions involving molecular or cluster ions. Thus, the present merged-beams experiment, together with the recent demonstration of a (near) single-quantum-state beam of molecular ions in the same apparatus [31], promise to open up a new era in the field of atomic and molecular collision physics. Worldwide there are three cryogenically cooled ion-beam storage rings in operation [27,33,34] where experiments with internally relaxed ions are performed [35]. Studies of single individual ion-ion interactions are, however, only possible in DESIREE.

### Mutual neutralization between $\text{Li}^+$ and $\text{D}^-$

The abundance of Li measured in stars is a key observation in astrophysics, providing information on stellar evolution and nucleosynthesis. For example, Li abundances measured in old, metal-poor stars probe the primordial Li produced in big-bang nucleosynthesis and processes occurring since [36–38]. Stellar Li abundances are deduced from observed spectra, preferably through radiative-collisional [non-local-thermodynamic-equilibrium (non-LTE)] modeling. Such modeling has shown that mutual neutralization between  $\text{Li}^+$  and  $\text{H}^-$  is an important collision process to be included for accurate interpretation of the Li I resonance line intensity and the Li abundance [39,40]. In the

present work we study the mutual neutralization reaction of  $\text{Li}^+$  and  $\text{D}^-$ ,



where  $\text{Li}^+$  and  $\text{D}^-$  are in their respective ground states before the collision. The final state,  $1s^2nl \ ^2L$  in Li, determines the kinetic-energy release,  $E_K(nl)$ , of the MN reaction in Eq. (1). For collisions at zero center-of-mass energy, the available energy in the reaction is the difference between the ionization energy of Li (5.39172 eV [41]) and the electron affinity of D (0.754579(87) eV [42]), which is about 4.64 eV. This amount of energy is too small to excite the D atom, but excitation in the Li atom is possible. Calculations suggest that the  $3s$ ,  $3p$ , and  $3d$  final states are completely dominating (see, for example, Ref. [43]). The corresponding kinetic-energy releases for populations of these states are 1.264, 0.803, and 0.759 eV, respectively. Until recently, there have been very few experimental studies of MN between  $\text{Li}^+$  and  $\text{D}^-$  ( $\text{H}^-$ ) [44,45]. In those two earlier studies, the MN cross sections were measured for center-of-mass energies between 33.3 and 2400 eV [44] and between 0.6 and 300 eV [45]. The final electron-capture states of Li were, however, not resolved. It is also important to study the process at lower center-of-mass energies, closer to the astrophysically relevant energy scale below 1 eV. Recently, in a single-pass experiment, Launoy *et al.* [32] measured final-state-resolved MN of  $\text{Li}^+$  and  $\text{D}^-$  for center-of-mass energies down to 3.9 meV where the  $3s$ ,  $3p$ , and  $3d$  states were resolved. Here, we present results at  $78 \pm 13$  meV and higher collision energies and compare the present branching fractions with those reported in Ref. [32]. The present experiment confirms the results of that study.

## II. EXPERIMENT

The DESIREE setup consists of two electrostatic ion-beam storage rings with 8.7-m circumferences and a 94.8-cm-long straight section referred to as the merging section, which is common to both rings and where the two stored ion beams overlap. The storage rings are enclosed in a single cryogenically cooled vacuum chamber, operating at 13 K with a residual gas density of only about  $10^4$   $\text{H}_2$  molecules per  $\text{cm}^3$  [27]. The setup is shown schematically in Fig. 1. In order to be able to merge two ion beams with different kinetic energies, one of the rings has been equipped with four additional deflectors such that the four quadrupole lenses have to be unevenly distributed around the ring. Because of this asymmetry, the ring is referred to as the asymmetric ring. The quadrupoles are evenly distributed around the other ring which is henceforth referred to as the symmetric ring. The ion beam with the highest kinetic energy is stored in the asymmetric ring. The initial-state collision energy in the center-of-mass frame,  $E_{\text{c.m.}}$ , for two particles  $A$  and  $B$ , with masses  $m_A$  and  $m_B$  and laboratory kinetic energies  $E_A$  and  $E_B$ , and with an angle  $\alpha$  between their trajectories is given by

$$E_{\text{c.m.}} = \mu \left[ \frac{E_A}{m_A} + \frac{E_B}{m_B} - 2\sqrt{\frac{E_A E_B}{m_A m_B}} \cos \alpha \right], \quad (2)$$

where  $\mu$  is the reduced mass of  $A$  and  $B$ . The beam energies, and thus the center-of-mass energy, can be controlled locally

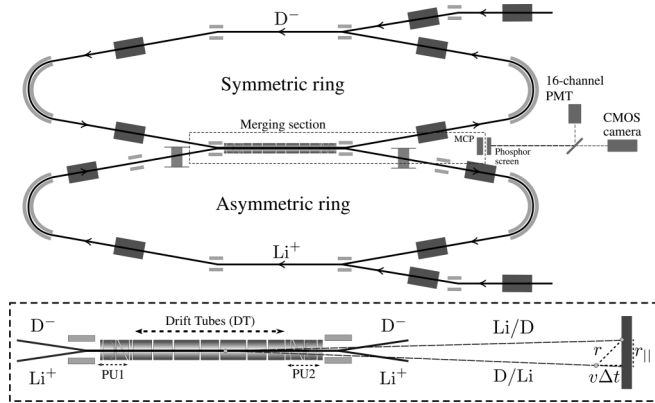


FIG. 1. Schematic of the DESIREE storage rings. The lower part shows the geometry of the merging section, and the experimental quantities are defined in the text.

by a system of up to seven drift tubes with a total length of 56 cm in the merging section. By biasing the drift tubes, one of the ion beams will be accelerated and the other beam, of ions in the opposite charge state, will be decelerated. With this setup,  $E_{c.m.}$  can be controlled in fine steps inside the drift tubes. Neutral products resulting from MN events inside the biased merging section are unaffected by the electrostatic fields and follow straight-line trajectories towards an imaging detector at a distance of 1.683 m from the center of the merging section. The imaging detector has a diameter of 74.9 mm, and consists of a triple-stack microchannel plate (MCP) with a phosphor-screen anode [46]. The light from the phosphor screen is guided by sets of optics through the windows of the DESIREE vacuum chambers to an optical beam splitter. As shown in Fig. 1, the transmitted light is directed at a CMOS camera, which is used to record the positions of the products on the detector. The reflected light is sent to a 16-channel photomultiplier tube (PMT). Two PMT signals from a single MN event are used to measure the difference in time of flight,  $\Delta t$ , between two neutrals triggering two different PMT channels.

In the present experiment,  $\text{Li}^+$  is produced in a Nielsen filament source [47], using a powder of  $\text{LiBr}$  heated in an oven. The  $\text{Li}^+$  ions are extracted from the source and accelerated to 17 keV. The  $\text{D}^-$  ions are produced in a SNICS ion source [48] using a solid  $\text{TiD}$  cathode, and accelerated to 6.5 keV. The choice of ion-beam energies is based on the expected collision energy in the unbiased parts of the merging section, and on the resulting arrival-time differences,  $\Delta t$ , of neutral pairs formed there. The nominal collision energy without a bias voltage on the drift tubes is close to  $E_{c.m.} = 93$  eV according to Eq. (2) for  $E_A = 17$  keV,  $E_B = 6.5$  keV, and  $\alpha = 0$ . The expected  $\Delta t$  for these events are of the order of hundreds of nanoseconds. For collisions close to  $E_{c.m.} = 0$  eV with a bias voltage on the merging section, the expected  $\Delta t$  values are much smaller and limited to tens of nanoseconds. Since the expected values of  $\Delta t$  differ by an order of magnitude with and without bias, it is straightforward to separate events that occurred in the biased part of the merging section from events in the unbiased part. For the present experiment, the three drift tubes in the center

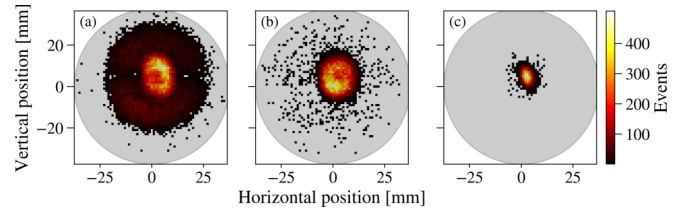


FIG. 2. Two-dimensional histograms of (a) the horizontal and vertical positions of  $\text{Li}$  and  $\text{D}$  products from  $\text{Li}^+ + \text{D}^-$  mutual neutralization reactions on the imaging detector, (b) the geometrical center positions of the two products, and (c) the center-of-mass position for events where the two products can be identified individually. The shaded area represents the physical size of the imaging detector, which has a diameter of 74.9 mm.

of the merging section are biased, resulting in an effective interaction region with a length of 24.4 cm.

Bunches of  $\text{Li}^+$  and  $\text{D}^-$  ions are injected at the same time in their respective rings. The positions of the ion beams are monitored using two sets of capacitive electrostatic pickups (PU1 and PU2 in Fig. 1). One pickup consists of two conductive cylinders, diagonally cut into two electrodes. One pair of electrodes is oriented in the horizontal direction and the other is oriented in the vertical direction. The voltage difference between opposing electrodes due to the image charges of the ion bunches provides a measure of the horizontal and vertical positions of the beams for the first approximately 50 ms until the bunches have spread out over the full ring circumference. The electrostatic ion optics in both rings are then used to optimize the overlap and trajectories of the two ion beams based on the measured beam positions before (PU1) and after (PU2) the merging section (see Fig. 1). For the present measurements and after optimizing the overlap, the ion beams are injected, and stored for 10 s, where the MN process is recorded continuously. After the storage, the ion beams are ejected from the rings, setting up for the next injection. For the present system, no explicit time dependence is expected in the MN signal, and the storage time of 10 s is based on the storage conditions of the ion beams.

### III. ANALYSIS AND RESULTS

As the MN products hit the imaging detector, the positions and time-of-flight differences  $\Delta t$  are recorded on an event-by-event basis. Before the data are analyzed in detail, we apply a set of selection criteria. Due to the finite resolution of the time-detection system, events with  $\Delta t < 3$  ns are rejected. In Fig. 2(a), we show a two-dimensional histogram of the positions of both MN products, where the two neutrals have been detected within 100 ns ( $\Delta t < 100$  ns). The high-intensity part in the center is primarily due to the heavier product ( $\text{Li}$ ) and MN events where both neutral products ( $\text{Li}$  and  $\text{D}$ ) travel close to the ion-beam axis. The outer, less intense part of the image consists mainly of neutral  $\text{D}$  atoms. For each event, the geometrical center position of the two particles on the detector is calculated, as shown in Fig. 2(b). If this position is too far away from the center of the image, the event is rejected. This selection allows for discrimination against false-coincidence events resulting from detector background. In Fig. 2(c), we

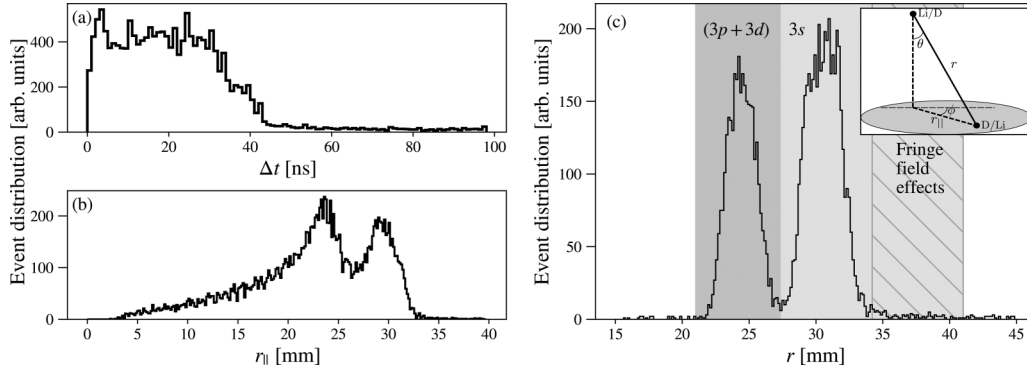


FIG. 3. Histograms of the  $\text{Li}^+ + \text{D}^- \rightarrow \text{Li}(nl) + \text{D}(1s)$  distribution measured at  $U_{\text{DT}} = -1295$  V in (a) difference in arrival time between the Li and D MN products,  $\Delta t$ ; (b) separation between the Li and D on the detector,  $r_{\parallel}$ ; and (c) neutral product separations  $r$ , as the first of the two particles (Li and D) hits the imaging detector. The  $3s$  channel is well separated from the  $3p$  and  $3d$  channels, while the  $3p$  and  $3d$  channels remain unresolved. The hatched area indicates events occurring in the fringe fields of the biased drift tubes. Inset: Definition of the angles  $\theta$  and  $\phi$  as described in the text.

show the position of the center of mass of the two products for events where the Li and D atoms were identified, based on the expected larger distance from the center of the image to the D atom.

A histogram of the distribution in  $\Delta t$  is shown in Fig. 3(a). This distribution is given by the kinetic-energy release and the direction of the interatomic vector after the reaction. The maximum  $\Delta t$  occurs when this direction is along the axis of the two ion beams. When the orientation is perpendicular to the axis of the two beams, the products hit the detector at the same time, resulting in  $\Delta t = 0$ . For each event, the distance between the products in the detector plane,  $r_{\parallel}$  (defined in Fig. 1), is deduced, and the distribution is shown in Fig. 3(b). The different final states can be associated with the two peaks at  $r_{\parallel} \sim 24$  mm and at  $r_{\parallel} \sim 30$  mm. To obtain a better separation of the final states, the information on  $\Delta t$  and  $r_{\parallel}$  can be combined to deduce the spatial separation,  $r$ , between the products as they hit the detector using  $r = \sqrt{r_{\parallel}^2 + (v\Delta t)^2}$ , where  $v$  is taken to be the average velocity of the two beams inside the biased drift tubes. Using the average velocity of the beams is an approximation that is valid as long as  $E_{\text{c.m.}}$  is small. For a correct calculation the velocity of the second product that hits the detector should be used, as indicated by the geometry in Fig. 1. The quantity  $r$  is the distance that the products have separated during their flight from the point of interaction to the detector. Hence  $r$  is independent of the final-state interatomic orientation. A histogram of the distribution in  $r$  is shown in Fig. 3(c). In addition to the selection criteria described above, the data in Fig. 3(c) have also undergone a selection based on the orientation between the products; these selection criteria will be described in detail in the following section.

#### A. Final-state distributions at the lowest center-of-mass energy

The center-of-mass energy,  $E_{\text{c.m.}}$ , is dependent on the velocities of the two ion beams, and the minimum  $E_{\text{c.m.}}$  is achieved when the velocities are equal for a given angle between the two ion-beam trajectories [see Eq. (2)]. For the present ion-beam energies, the velocities should be equal in the biased part of the merging section when  $U_{\text{DT}} = -1277$  V.

In order to find the minimum  $E_{\text{c.m.}}$  experimentally, the drift tube voltage is scanned until the maximum MN rate is observed. The MN cross section is approximately  $\sigma \propto 1/E_{\text{c.m.}}$  [49]; thus, the rate should have a maximum at the minimum  $E_{\text{c.m.}}$ . The resulting experimental minimum of  $E_{\text{c.m.}}$  was found at  $U_{\text{DT}} = -1295$  V. The difference between the calculated (ideal) and measured  $U_{\text{DT}}$  value for the minimum  $E_{\text{c.m.}}$  is ascribed to uncertainties in the measurements of the ion-beam energies and the drift tube bias voltage. In Fig. 3(c), we show a histogram of  $r$  measured at  $U_{\text{DT}} = -1295$  V. There is a clear separation between the  $3s$  (peak at high  $r$ ) and the  $3p$  and  $3d$  final states (peak at low  $r$ ). As expected from the experimental resolution, which is limited by the ratio between the length of the biased interaction region and the distance to the detector, it is not possible to resolve the  $3p$  and  $3d$  states.

From the scan of the drift tube voltage it is also possible to measure the initial-state collision energy,  $E_{\text{c.m.}}$ , as a function of  $U_{\text{DT}}$ . The total kinetic energy in the center-of-mass system after an MN event is

$$E_{\text{c.m.}} + E_{\text{K}}(nl) = \frac{\mu}{2} \left( \frac{r_{nl}v}{L} \right)^2, \quad (3)$$

where  $L$  is the distance between the imaging detector and the point in the merging section where the MN event occurred and  $r_{nl}$  is the separation between the MN products for the final state  $nl$  in Li. Since it is not possible to determine at which point the MN event took place, an average value of  $L$ ,  $\bar{L} = 1.683 \pm 0.010$  m, is taken as the distance from the center of the merging section to the imaging detector. The uncertainty in  $\bar{L}$  is mainly ascribed to the variation in the overlap between the two beams along their common section. For each value of  $U_{\text{DT}}$ , an  $r$  distribution corresponding to the one shown for  $U_{\text{DT}} = -1295$  V in Fig. 3(c) is deduced. From these distributions, average values,  $\bar{r}_{nl}$ , for the  $3s$  channel separately and for the  $3p$  and the  $3d$  channels together are extracted. Since the  $E_{\text{K}}(nl)$  values are known, an average initial-state center-of-mass energy  $\bar{E}_{\text{c.m.}}$  can be deduced from  $v$ ,  $\bar{L}$ , and the  $\bar{r}_{nl}$  values using Eq. (3). In Fig. 4, we show the experimental values of  $\bar{E}_{\text{c.m.}}$  as a function of  $U_{\text{DT}}$ . The solid line in Fig. 4 is a fit to Eq. (2) with the average angle between  $\text{Li}^+$  and  $\text{D}^-$  trajectories before the collision,  $\bar{\alpha}$ , and a

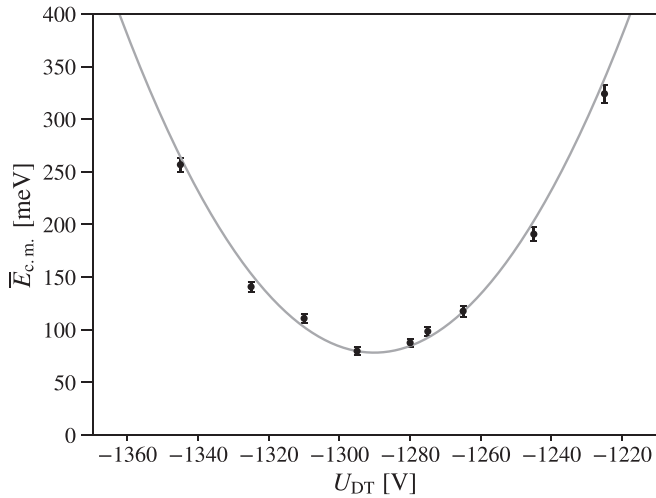


FIG. 4. Measured average initial-state center-of-mass  $\text{Li}^+ + \text{D}^-$  collision energy,  $\bar{E}_{\text{c.m.}}$ , as a function of drift tube voltage  $U_{\text{DT}}$ . The solid line is a fit to Eq. (2).

voltage offset as free parameters. The fit yields  $\bar{\alpha} = 4.1 \pm 0.1$  mrad, and applying the fitted model to the measurement in Fig. 3(c) we get  $\bar{E}_{\text{c.m.}} = 78$  meV with a *statistical* uncertainty of 3 meV, resulting from the statistical errors in the fit in Fig. 4. The uncertainty in  $\bar{L}$  is considered a systematic uncertainty, which is included by treating  $\bar{L}$  as a parameter in the analysis and performing the fit described above for different values of  $\bar{L}$  within the interval defined by its uncertainty. Adding the systematic uncertainties in quadrature with the statistical uncertainties given above we get  $\bar{\alpha} = 4.1 \pm 0.4$  mrad and  $\bar{E}_{\text{c.m.}} = 78 \pm 13$  meV for the measurement in Fig. 3(c).

The data in Fig. 3(c) can be used to determine the branching fraction between the  $3s$  state, on one hand, and the  $3p$  and  $3d$  states together, on the other hand. However, a number of systematic effects must be taken into account. In Fig. 2(a), there is a lower density of events along the horizontal axis near the center of the image. This effect is due to a limitation in the ability to measure time differences with the 16-channel PMT. In order to obtain a time difference from an MN event, the neutral products must trigger two different channels of the PMT. If the final-state interatomic orientation is predominantly in the horizontal plane, both products will hit the same channel on the PMT and no time difference can be extracted. The probability of both neutrals triggering the same channel on the PMT increases with decreasing kinetic-energy release. Accounting for this systematic effect is important and the correction is made by introducing selection criteria based on the angles between the interatomic axis, the normal to the detector surface, and the direction along which the PMT channels are oriented (the horizontal plane). This is indicated in the inset in Fig. 3(c). The azimuthal angle,  $\phi$ , is defined as the angle between a line connecting the Li and D positions in the detector plane and a line parallel to the horizontal axis of the detector. The polar angle,  $\theta$ , is the angle between the line connecting the two products as they hit the detector and the normal to the detector plane as shown in the inset of Fig. 3(c). For collisions at low center-of-mass energies, the intensities as functions of  $\phi$  and  $\cos\theta$  are expected to be uniformly

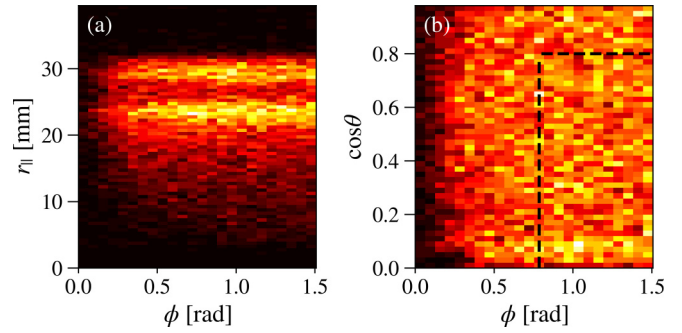


FIG. 5. Two-dimensional histograms. (a) The azimuthal angle  $\phi$  and the distance between products in the detector plane,  $r_{\perp}$ . A decrease in signal at small  $\phi$  is clearly visible and is due to a higher probability for Li and D to hit the same PMT channel. (b) The azimuthal angle,  $\phi$ , and  $\cos\theta$ , where  $\theta$  is the polar angle. The dashed lines show the selected region ( $\phi > \pi/4$  and  $\cos\theta < 0.8$ ) used in the spectrum in Fig. 3(c).

distributed on the intervals  $0$  to  $\pi/2$ , and  $0$  to  $1$ , respectively. For small  $\phi$ , a large fraction of the MN products will trigger the same PMT channel, resulting in fewer events as shown in Fig. 5. The distribution in  $\cos\theta$  is close to uniform over the whole range. However, events with  $\cos\theta$  close to  $1$  are largely due to collisions at higher center-of-mass energies (i.e., to collisions occurring in the fringe fields of the two outer biased drift tubes), resulting in additional background at the higher end of the  $r$  spectrum. By selecting events with  $\cos\theta < 0.8$  this background is significantly reduced. The distribution in  $\phi$  and  $\cos\theta$  is shown in Fig. 5(b), and the additional selection criteria are indicated by the dashed lines.

The orientation-based selection criteria described above are sufficient to account for the systematic effects due to the detection system. While important in principle, the correction is less than 1% for the  $3s$  branching fraction. The data in Fig. 3(c) can thus be used to determine the branching fraction for the  $3s$  final state. The channels are well separated in the spectrum, but due to the small background contribution between the channels, the choice of intervals in  $r$  that defines the  $3s$  state and the  $(3p + 3d)$  states introduces a small systematic uncertainty. The intervals chosen are indicated by the shaded areas in Fig. 3(c). The systematic uncertainty is estimated by determining the branching fraction for different choices of the intervals, and it is estimated to be 0.4%. At  $r$  values below the  $(3p + 3d)$  channels, there is a small background contribution that does not affect the measured branching fraction. At  $r$  values above the  $3s$  peak, there is a significant background contribution. The background is due to collisions at higher center-of-mass energies resulting from reactions taking place in the fringe fields at the entrance and exit of the biased drift tubes. These higher-energy collisions predominantly yield higher values of  $r$ , causing the number of events in the  $3s$  channel to be overestimated. This background contribution present in the  $3s$  interval is accounted for by subtracting the total background contribution on the interval indicated by the hatched area in Fig. 3(c) from the  $3s$  signal. The underlying assumption is that the background contribution from the  $3s$  channel is approximately equal to the background contribution from the  $(3p + 3d)$  channels, which is reasonable since

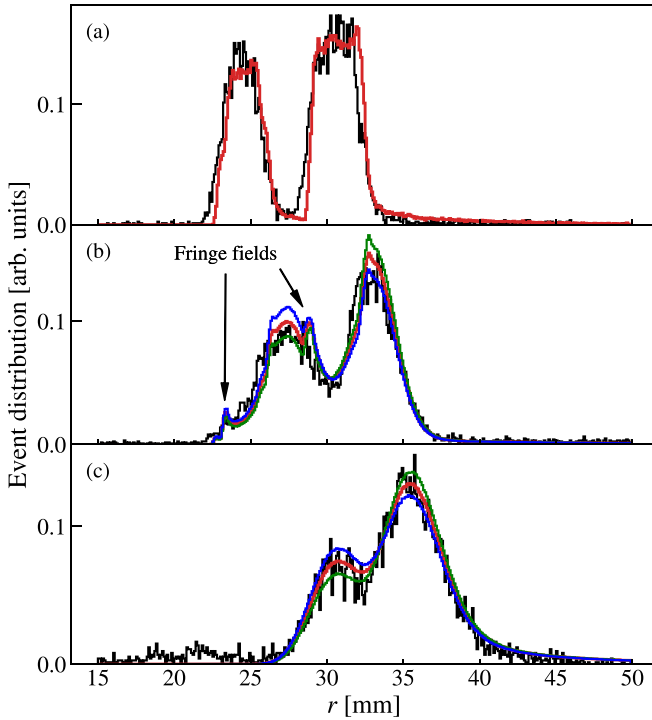


FIG. 6. Histograms of  $r$  for  $\text{Li}^+ + \text{D}^- \rightarrow \text{Li}(nl) + \text{D}(1s)$  recorded at (a)  $\bar{E}_{c.m.} = 78 \pm 13$  meV, (b)  $\bar{E}_{c.m.} = 262 \pm 15$  meV, and (c)  $\bar{E}_{c.m.} = 630 \pm 17$  meV. The measurements are compared to Monte Carlo simulations (red, blue, and green curves) as described in the text.

the branching fractions are similar for the  $3s$  and  $(3p + 3d)$  channels. From these considerations we obtain the branching fraction (BF) for the  $3s$  state,  $\text{BF}(3s) = 57.8 \pm 0.6\%$ , where the uncertainty refers to the statistical uncertainty. By adding the statistical and systematic uncertainties in quadrature we obtain the final result for the branching fraction of the  $3s$  final state,  $\text{BF}(3s) = 57.8 \pm 0.7\%$ , at a center-of-mass energy of  $78 \pm 13$  meV.

### B. Final-state distributions at higher center-of-mass energies

In addition to the data at different  $\bar{E}_{c.m.}$  shown in Fig. 4, spectra were measured with high statistics at  $U_{DT} = -1345$  V and at  $U_{DT} = -1195$  V. The corresponding center-of-mass energies obtained from the fit in Fig. 4 are  $\bar{E}_{c.m.} = 262 \pm 15$  meV and  $\bar{E}_{c.m.} = 630 \pm 17$  meV, respectively. The measured spectra are shown in Fig. 6, along with the spectrum at  $\bar{E}_{c.m.} = 78 \pm 13$  meV. As the center-of-mass energy increases, the different final states are no longer fully resolved. The decreased resolution is due to the approximations used in the calculation of  $r$ , as well as the spread in the energies of the two ion beams. When the channels are no longer separated, it is not possible to determine the branching fraction by counting the number of events as for  $\bar{E}_{c.m.} = 78 \pm 13$  meV in Fig. 3(c). Furthermore, when the collision energy increases, the distribution in  $\cos \theta$  is no longer expected to be uniform, and the angular selection described previously is not possible.

In order to be able to extract information on the branching fractions also from the results for  $\bar{E}_{c.m.} = 262 \pm 15$  meV and

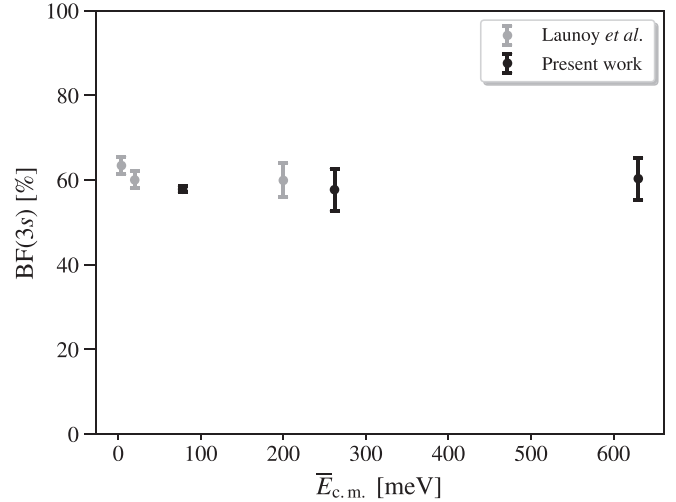


FIG. 7. Measured  $3s$  branching fractions for the  $\text{Li}^+ + \text{D}^- \rightarrow \text{Li}(nl) + \text{D}(1s)$  reaction as a function of center-of-mass energy  $\bar{E}_{c.m.}$ . The black data points are the present results and the gray data points are the measurements by Launoy *et al.* [32].

$\bar{E}_{c.m.} = 630 \pm 17$  meV, we have performed Monte Carlo simulations. The simulations are performed on an event-by-event basis where the probabilities of the different product channels are given by assumed branching fractions as described in the following. The initial kinetic energies of the ions are assumed to follow a Gaussian distribution centered at the beam energy, and with a standard deviation of 0.2% of the mean value of the distribution. The potential as a function of position in the drift tubes is modeled using SIMION [50]. For each MN event,  $E_{c.m.}$  is calculated and the event is accepted with a probability proportional to  $1/\sqrt{E_{c.m.}}$  to account for the energy dependence of the rate coefficient. The flight times of the products as well as their final positions on the detector are calculated, and the resulting  $r$  spectra are constructed and compared with the experimental data. In Fig. 6(a), we show a simulation performed using the  $3s$  branching fraction of  $57.8 \pm 0.7\%$  measured at  $\bar{E}_{c.m.} = 78 \pm 13$  meV. For the simulations at higher collision energies, shown by the red curves in Figs. 6(b) and 6(c), the branching fractions are extracted by minimizing the sum of the squared residuals between the data and simulation, as a function of the assumed  $3s$  branching fraction. This procedure results in  $3s$  branching fractions of  $57.7 \pm 5.0\%$  at  $\bar{E}_{c.m.} = 262 \pm 15$  meV and  $60.3 \pm 5.0\%$  at  $\bar{E}_{c.m.} = 630 \pm 17$  meV, where the uncertainties are estimated by comparing the simulated spectra to the data. The blue and green curves in Figs. 6(b) and 6(c) are the results of simulations where the assumed  $3s$  branching fraction corresponds to the limits ( $\pm 5\%$ ) of the intervals given by the indicated error estimates. The additional structures in the simulated data in Fig. 6(b) below  $r = 25$  mm and at  $r \approx 28$  mm result from a section of the drift tubes where the fringe fields result in a lower collision energy. To understand this effect we consider the bias voltage as a continuous function of the position in the drift tubes, varying between 0 and  $-1345$  V. From Fig. 4 it is then clear that at some point in the fringe fields the center-of-mass energy is at the minimum. This effect is not present in Fig. 6(c), since  $U_{DT} = -1195$  V is to the right of the minimum in Fig. 4,

and therefore the center-of-mass energies for collisions in the fringe fields will be higher than at  $-1195$  V.

The measured  $3s$  branching fractions for  $\text{Li}^+ + \text{D}^-$  at low collision energies,  $\bar{E}_{\text{c.m.}}$ , are summarized in Fig. 7 and include the results of Launoy *et al.* [32]. Combining the results using the two different techniques suggests that the branching fraction varies little in the energy region below about 1 eV. A consequence of performing the experiment with stored beams is that larger beam apertures are needed than in a single-pass experiment. Due to the influence of fringe field effects, this means that also the length of the biased section where the low controlled relative velocity is obtained must be longer. As the measured entity is the distance between the two neutrals as they reach the detector, this increased uncertainty in the position where the reaction took place translates into a somewhat poorer resolution. On the other hand, DESIREE has the unique advantage that it will be possible to prepare molecular and cluster ions in single or narrow ranges of rovibrational states before the interactions.

#### IV. CONCLUSION AND OUTLOOK

In this work we have shown that merged-beams ion-ion collision studies may be performed by means of cryogenically cooled, electrostatic, ion-beam storage rings and that different final states could be resolved. The present pilot experiment was performed with atomic ions,  $\text{Li}^+$  ( $1s^2$ ) and  $\text{D}^-$  ( $1s^2$ ), and the final electron-capture states in neutral Li were partly resolved such that the  $3s$  state was separated from the unresolved  $3p$  and  $3d$  states at a center-of-mass  $\text{Li}^+ + \text{D}^-$

collision energy of  $78 \pm 13$  meV. The ability to store the ions for extended periods of time allows for future studies where excited metastable states in atomic, molecular, and cluster ions have time to relax before the stored ions are allowed to interact. With this technique it will thus be possible to perform merged-beams experiments with simple and complex molecular and cluster ions in their lowest vibrational and rotational states. Ways to improve the energy resolution, and to go lower in collision energy, are now being implemented through a better control of the angle between the stored ion beams in the merging section.

#### ACKNOWLEDGMENTS

This work was performed at the Swedish National Infrastructure, DESIREE (Swedish Research Council Contract No. 2017-00621). It is a part of the project ‘‘Probing charge- and mass-transfer reactions on the atomic level,’’ supported by the Knut and Alice Wallenberg Foundation (Grant No. 2018.0028). Furthermore, H.C., H.Z., P.S.B., and H.T.S. thank the Swedish Research Council for individual project grants (with Contracts No. 2019-04379, No. 2016-04181, No. 2016-03765, and No. 2018-04092). This material is based upon work supported by the Air Force Office of Scientific Research under Award No. FA9550-19-1-7012. P.S.B. and J.G. would like to acknowledge financial support from the project grant ‘‘The New Milky Way’’ (Grant No. 2013.0052) from the Knut and Alice Wallenberg Foundation.

- 
- [1] L. H. Thomas, On the capture of electrons by moving electrified particles, *Proc. R. Soc. London Ser. A* **114**, 561 (1927).
  - [2] J. R. Oppenheimer, On the quantum theory of the capture of electrons, *Phys. Rev.* **31**, 349 (1928).
  - [3] C. M. Lisse, K. Dennerl, J. Englhauser, M. Harden, F. E. Marshall, M. J. Mumma, R. Petre, J. P. Pye, M. J. Ricketts, J. Schmitt, J. Trümper, and R. G. West, Discovery of x-ray and extreme ultraviolet emission from comet C/Hyakutake 1996 B2, *Science* **274**, 205 (1996).
  - [4] P. Chaizy, H. Reme, J. Sauvaud, C. d’Uston, R. Lin, D. Larson, D. Mitchell, K. Anderson, C. Carlson, A. Korth *et al.*, Negative ions in the coma of comet Halley, *Nature (London)* **349**, 393 (1991).
  - [5] E. Zipf, P. Espy, and C. Boyle, The excitation and collisional deactivation of metastable  $n(2p)$  atoms in auroras, *J. Geophys. Res.* **85**, 687 (1980).
  - [6] M. H. Rees and R. G. Roble, Excitation of  $\text{O}(^1D)$  atoms in aurorae and emission of the  $[\text{OI}]$  6300-Å line, *Can. J. Phys.* **64**, 1608 (1986).
  - [7] D. Koutroumpa, R. Lallement, V. Kharchenko, A. Dalgarno, R. Pepino, V. Izmodenov, and E. Quémerais, Charge-transfer induced EUV and soft x-ray emissions in the heliosphere, *A&A* **460**, 289 (2006).
  - [8] D. Koutroumpa, F. Acero, R. Lallement, J. Ballet, and V. Kharchenko, OVII and OVIII line emission in the diffuse soft x-ray background: Heliospheric and galactic contributions, *A&A* **475**, 901 (2007).
  - [9] E. Möbius, D. Rucinski, D. Hovestadt, and B. Klecker, The helium parameters of the very local interstellar medium as derived from the distribution of  $\text{He}^+$  pickup ions in the solar wind, *A&A* **304**, 505 (1995).
  - [10] R. C. Isler, An overview of charge-exchange spectroscopy as a plasma diagnostic, *Plasma Phys. Controlled Fusion* **36**, 171 (1994).
  - [11] S. S. Prasad and W. T. Huntress, Jr., A model for gas phase chemistry in interstellar clouds: I. The basic model, library of chemical reactions, and chemistry among C, N, and O compounds., *Astrophys. J. Suppl. Ser.* **43**, 1 (1980).
  - [12] A. Yoshimori, T. Kakitani, Y. Enomoto, and N. Mataga, Shapes of the electron-transfer rate vs energy gap relations in polar solutions, *J. Phys. Chem. C* **93**, 8316 (1989).
  - [13] D. Goodhead, Initial events in the cellular effects of ionizing radiations: Clustered damage in DNA, *Int. J. Radiat. Biol.* **65**, 7 (1994).
  - [14] F. Aumayr, K. Ueda, E. Sokell, S. Schippers, H. Sadeghpour, F. Merkt, T. F. Gallagher, F. B. Dunning, P. Scheier, O. Echt, T. Kirchner, S. Fritzsche, A. Surzhykov, X. Ma, R. Rivarola, O. Fojon, L. Tribedi, E. Lamour, J. R. C. López-Urrutia, Y. A. Litvinov, V. Shabaev, H. Cederquist, H. Zettergren, M. Schlegelberger, R. A. Wilhelm, T. Azuma, P. Boduch, H. T.

- Schmidt, and T. Stöhlker, Roadmap on photonic, electronic and atomic collision physics: III. heavy particles: With zero to relativistic speeds, *J. Phys. B: At. Mol. Opt. Phys.* **52**, 171003 (2019).
- [15] C. Chin, R. Grimm, P. Julienne, and E. Tiesinga, Feshbach resonances in ultracold gases, *Rev. Mod. Phys.* **82**, 1225 (2010).
- [16] E. Herbst and E. F. van Dishoeck, Complex organic interstellar molecules, *Annu. Rev. Astron. Astrophys.* **47**, 427 (2009).
- [17] A. G. G. M. Tielens, The molecular universe, *Rev. Mod. Phys.* **85**, 1021 (2013).
- [18] J. Ullrich, R. Moshhammer, A. Dorn, R. Dörner, L. P. H. Schmidt, and H. Schmidt-Böcking, Recoil-ion and electron momentum spectroscopy: Reaction microscopes, *Rep. Prog. Phys.* **66**, 1463 (2003).
- [19] R. Dörner, V. Mergel, O. Jagutzki, L. Spielberger, J. Ullrich, R. Moshhammer, and H. Schmidt-Böcking, Cold target recoil ion momentum spectroscopy: A “momentum microscope” to view atomic collision dynamics, *Phys. Rep.* **330**, 95 (2000).
- [20] E. Horsdal-Pedersen, C. L. Cocke, and M. Stockli, Experimental Observation of the Thomas Peak in High-Velocity Electron Capture by Protons from He, *Phys. Rev. Lett.* **50**, 1910 (1983).
- [21] D. Fischer, M. Gudmundsson, Z. Berényi, N. Haag, H. A. B. Johansson, D. Misra, P. Reinhed, A. Källberg, A. Simonsson, K. Stöckel, H. Cederquist, and H. T. Schmidt, Importance of Thomas single-electron transfer in fast *p*-He collisions, *Phys. Rev. A* **81**, 012714 (2010).
- [22] R. Stensgaard, ASTRID—the Aarhus storage ring, *Phys. Scr.* **T22**, 315 (1988).
- [23] P. Baumann, M. Blum, A. Friedrich, C. Geyer, M. Grieser, B. Holzer, E. Jaeschke, D. Krämer, C. Martin, K. Matl, R. Mayer, W. Ott, B. Povh, R. Repnow, M. Steck, E. Steffens, and W. Arnold, The Heidelberg heavy ion test storage ring TSR, *Nucl. Instrum. Methods Phys. Res., Sect. A* **268**, 531 (1988).
- [24] K. Abrahamsson, G. Andler, L. Bagge, E. Beebe, P. Carlé, H. Danared, S. Egnell, K. Ehrnsten, M. Engström, C. Herrlander *et al.*, CRYRING—a synchrotron, cooler and storage ring, *Nucl. Instrum. Methods Phys. Res., Sect. B* **79**, 269 (1993).
- [25] B. Franzke, The heavy ion storage and cooler ring project ESR at GSI, *Nucl. Instrum. Methods Phys. Res., Sect. B* **24-25**, 18 (1987).
- [26] H. Danared, G. Andler, L. Bagge, C. J. Herrlander, J. Hilke, J. Jeansson, A. Källberg, A. Nilsson, A. Paál, K. G. Rensfelt, U. Rosengård, J. Starker, and M. af Ugglas, Electron Cooling with an Ultracold Electron Beam, *Phys. Rev. Lett.* **72**, 3775 (1994).
- [27] R. D. Thomas, H. T. Schmidt, G. Andler, M. Björkhage, M. Blom, L. Brännholm, E. Bäckström, H. Danared, S. Das, N. Haag *et al.*, The double electrostatic ion ring experiment: A unique cryogenic electrostatic storage ring for merged ion-beams studies, *Rev. Sci. Instrum.* **82**, 065112 (2011).
- [28] H. T. Schmidt, R. D. Thomas, M. Gatchell, S. Rosén, P. Reinhed, P. Löfgren, L. Brännholm, M. Blom, M. Björkhage, E. Bäckström *et al.*, First storage of ion beams in the double electrostatic ion-ring experiment: DESIREE, *Rev. Sci. Instrum.* **84**, 055115 (2013).
- [29] N. de Ruelle, A. Dochain, T. Launoy, R. F. Nascimento, M. Kaminska, M. H. Stockett, N. Vaeck, H. T. Schmidt, H. Cederquist, and X. Urbain, Mutual Neutralization of O<sup>-</sup> with O<sup>+</sup> and N<sup>+</sup> at Subthermal Collision Energies, *Phys. Rev. Lett.* **121**, 083401 (2018).
- [30] E. Bäckström, D. Hanstorp, O. M. Hole, M. Kaminska, R. F. Nascimento, M. Blom, M. Björkhage, A. Källberg, P. Löfgren, P. Reinhed, S. Rosén, A. Simonsson, R. D. Thomas, S. Mannervik, H. T. Schmidt, and H. Cederquist, Storing keV Negative Ions for an Hour: The Lifetime of the Metastable <sup>2</sup>P<sub>1/2</sub><sup>o</sup> Level in <sup>32</sup>S<sup>-</sup>, *Phys. Rev. Lett.* **114**, 143003 (2015).
- [31] H. T. Schmidt, G. Eklund, K. C. Chartkunchand, E. K. Anderson, M. Kamińska, N. de Ruelle, R. D. Thomas, M. K. Kristiansson, M. Gatchell, P. Reinhed *et al.*, Rotationally Cold OH<sup>-</sup> Ions in the Cryogenic Electrostatic Ion-Beam Storage Ring DESIREE, *Phys. Rev. Lett.* **119**, 073001 (2017).
- [32] T. Launoy, J. Loreau, A. Dochain, J. Liévin, N. Vaeck, and X. Urbain, Mutual neutralization in Li<sup>+</sup>-D<sup>-</sup> collisions: A combined experimental and theoretical study, *Astrophys. J.* **883**, 85 (2019).
- [33] R. von Hahn, A. Becker, F. Berg, K. Blaum, C. Breitenfeldt, H. Fadil, F. Fellenberger, M. Froese, S. George, J. Göck *et al.*, The cryogenic storage ring CSR, *Rev. Sci. Instrum.* **87**, 063115 (2016).
- [34] Y. Nakano, Y. Enomoto, T. Masunaga, S. Menk, P. Bertier, and T. Azuma, Design and commissioning of the RIKEN cryogenic electrostatic ring (RICE), *Rev. Sci. Instrum.* **88**, 033110 (2017).
- [35] O. Novotný, P. Wilhelm, D. Paul, Á. Kálosi, S. Saurabh, A. Becker, K. Blaum, S. George, J. Göck, M. Grieser *et al.*, Quantum-state-selective electron recombination studies suggest enhanced abundance of primordial HeH<sup>+</sup>, *Science* **365**, 676 (2019).
- [36] W. Aoki, P. S. Barklem, T. C. Beers, N. Christlieb, S. Inoue, A. E. G. Pérez, J. E. Norris, and D. Carollo, Lithium abundances of extremely metal-poor turnoff stars, *Astrophys. J.* **698**, 1803 (2009).
- [37] B. D. Fields, The primordial lithium problem, *Annu. Rev. Nucl. Part. Sci.* **61**, 47 (2011).
- [38] A. J. Korn, F. Grundahl, O. Richard, P. Barklem, L. Mashonkina, R. Collet, N. Piskunov, and B. Gustafsson, A probable stellar solution to the cosmological lithium discrepancy, *Nature (London)* **442**, 657 (2006).
- [39] W. Steenbock and H. Holweger, Statistical equilibrium of lithium in cool stars of different metallicity, *A&A* **130**, 319 (1984).
- [40] P. S. Barklem, A. Belyaev, and M. Asplund, Inelastic H+Li and H<sup>-</sup>+Li<sup>+</sup> collisions and non-LTE Li I line formation in stellar atmospheres, *Astron. Astrophys.* **409**, L1 (2003).
- [41] Ionization potentials of atoms and atomic ions, in *CRC Handbook of Chemistry and Physics, Internet Version 2005*, edited by D. R. Lide (CRC Press, Boca Raton, FL, 2005).
- [42] K. R. Lykke, K. K. Murray, and W. C. Lineberger, Threshold photodetachment of H<sup>-</sup>, *Phys. Rev. A* **43**, 6104 (1991).
- [43] H. Croft, A. S. Dickinson, and F. X. Gadéa, A theoretical study of mutual neutralization in Li<sup>+</sup>+H<sup>-</sup> collisions, *J. Phys. B: At. Mol. Opt. Phys.* **32**, 81 (1999).

- [44] B. Peart and S. J. Foster, Measurements of mutual neutralisation of  $\text{Li}^+$  with  $\text{H}^-$  ions and of  $\text{Na}^+$  with  $\text{O}^-$  ions, *J. Phys. B: At. Mol. Phys.* **20**, L691 (1987).
- [45] B. Peart and D. A. Hayton, Merged beam measurements of the mutual neutralization of  $\text{He}^+/\text{H}^-$  and  $\text{Li}^+/\text{D}^-$  ions, *J. Phys. B: At. Mol. Opt. Phys.* **27**, 2551 (1994).
- [46] S. Rosén, H. T. Schmidt, P. Reinhed, D. Fischer, R. D. Thomas, H. Cederquist, L. Liljeby, L. Bagge, S. Leontein, and M. Blom, Operating a triple stack microchannel plate-phosphor assembly for single particle counting in the 12–300 K temperature range, *Rev. Sci. Instrum.* **78**, 113301 (2007).
- [47] K. O. Nielsen, The development of magnetic ion sources for an electromagnetic isotope separator, *Nucl. Instrum.* **1**, 289 (1957).
- [48] SNICS, Source of Negative Ions by Cesium Sputtering, National Electrostatics Corporation.
- [49] G. W. Drake, *Springer Handbook of Atomic, Molecular, and Optical Physics* (Springer, New York, 2006).
- [50] D. A. Dahl, SIMION3D version 6.0 users manual, EG and G Idaho, Inc., Idaho Falls, ID, 1995 (unpublished).